Materials Today Energy 29 (2022) 101110

Contents lists available at ScienceDirect

Materials Today Energy

journal homepage: www.journals.elsevier.com/materials-today-energy/

Zn(II) and Cu(II) tetrakis(diarylamine)phthalocyanines as hole-transporting materials for perovskite solar cells

Nadja Klipfel [a], Jianxing Xia [a], Pavel Čulík [a], Simonetta Orlandi [b], Marco Cavazzini [b], Naoyuki Shibayama [c], Hiroyuki Kanda [a], Cansu Igci [a], Wei Li [d], Yi-Bing Cheng [d], Vygintas Jankauskas [e], Kristijonas Genevicius [e], Abdullah M. Asiri [f], Cristina Momblona [a, ***], Kasparas Rakstys [e], Gianluca Pozzi [b, **], Mohammad Khaja Nazeeruddin [a, g, *]

[a] Group for Molecular Engineering of Functional Materials, Institute of Chemical Sciences and Engineering, École Polytechnique Fédérale de Lausanne, Valais Wallis, Rue de l'Industrie 17, 1950, Sion, Switzerland
[b] CNR Institute of Chemical Sciences and Technologies "Giulio Natta" (CNR SCITEC), UOS Golgi, via Golgi 19, 20133, Milan, Italy
[c] Department of Biomedical Engineering, Toin University of Yokohama, 1614 Kurogane, Aoba, Yokohama, Japan
[d] Foshan Xianhu Laboratory of the Advanced Energy Science and Technology Guangdong Laboratory, Xianhu Hydrogen Valley, Foshan, People's Republic of China
[e] Department of Organic Chemistry, Kaunas University of Technology, Radvilenu pl. 19, Kaunas, 50254, Lithuania
[f] Center of Excellence for Advanced Materials Research (CEAMR), King Abdulaziz University, P.O. Box 80203, 21589, Jeddah, Saudi Arabia
[g] Department of Materials Science and Engineering, City University of Hong Kong, Kowloon, Hong Kong

ARTICLE INFO

Article history:
Received 14 March 2022
Received in revised form
29 July 2022
Accepted 30 July 2022
Available online 14 August 2022

Keywords:
Zn-phthalocyanines
Spin-coating
Diarylamine
Functionalization
Alkoxy chains

ABSTRACT

Finding new hole-transporting materials (HTMs) suitable for replacing the state-of-the-art **spiro-OMeTAD** is still challenging. In this work, newly synthesized diarylamine-substituted metal phthalocyanines (MPcs, M = Zn(II) or Cu(II)) functionalized with either linear or branched alkoxy chains are evaluated as HTMs in perovskite solar cells. Both the nature of the alkoxy chains and that of the coordinated metal species were found to influence the functional properties of the new MPcs. In particular, devices based on a ZnPc featuring four *n*-butoxy side chains exhibited the highest power conversion efficiencies (PCEs). A PCE of 20.00% was reached for triple cation perovskite devices, and a PCE up to 20.18% could be achieved for double cation devices.

1. Introduction

The power conversion efficiency (PCE) of perovskite solar cells (PSCs) increased over the last decade, from 3.8% to over 25% [1,2], making PSCs a promising technology toward reduced carbon emissions [3], with additional benefits in terms of sustainability goals, such as low cost [4], ease of fabrication, and recyclability [5]. The remarkable increase in PSCs efficiency was achieved by carefully optimizing the perovskite composition and improving the electron- [6,7] hole- [8,9] transporting layers. Nevertheless, the commercialization of PSCs is still challenging due to the instability of the overall device and the material itself towards heat, stress humidity, light illumination, and oxygen [10–13]. Some instability can also be originated from the chemical doping of the hole-transporting material (HTM). In *n-i-p* PSCs, the HTM is typically sandwiched between the perovskite layer and the metal top electrode. Therefore, the energy-alignment between the highest occupied molecular orbital (HOMO) and the perovskite valence band (VB) is essential for an efficient hole-extraction, ensuring good transport towards the electrode [14,15]. Despite the effort to find new hole-transporting materials that improve the perovskite solar cell in stability and efficiency, 2,2′,7,7′-Tetrakis[N,N-di(4-

* Corresponding author. Group for Molecular Engineering of Functional Materials, Institute of Chemical Sciences and Engineering, École Polytechnique Fédérale de Lausanne, Valais Wallis, Rue de l'Industrie 17, 1950, Sion, Switzerland.
** Corresponding author.
*** Corresponding author.
E-mail addresses: cristina.momblonarincon@epfl.ch (C. Momblona), gianluca.pozzi@scitec.cnr.it (G. Pozzi), mdkhaja.nazeeruddin@epfl.ch (M.K. Nazeeruddin).

https://doi.org/10.1016/j.mtener.2022.101110

methoxyphenyl)amino]-9,9′-spirobifluorene (**spiro-OMeTAD**) is still the benchmark HTM, even though drawbacks such as high costs, low intrinsic conductivity, and hole-mobility and stability are well known and limit the potential in up-scaling of the technology [9,16,17].

Phthalocyanines (Pcs) are structurally related to porphyrins, which are photo- and electrochemically stable [18]. Several transition metal complexes of phthalocyanines (MPcs) endowed with semiconducting properties in the solid-state have been investigated in recent years as HTMs in PSCs [19]. The unsubstituted CuPcs complex was vacuum-deposited and employed as HTM in PSCs, leading to device efficiencies ranging from 5.0% to 15.4% [20,21]. Efforts to improve the efficiency of the stability of the devices employing CuPcs ranged from post-treating the perovskite layer with a solvent and vapor treatment [22], integrating an Au contact electrode and C_{60} HTM into the device [21]. Lui et al. demonstrated shortly after, that the more expensive materials used before could be replaced by a low-temperature printable carbon electrode and a TiO_2/SnO_2 bilayer [23]. Different studies were also conducted for implementing the CuPcs in p-i-n configuration. Changing the perovskite composition from $MAPBI_3$ to CsFAMA lead to an improved efficiency [24], and the introductions of vanadium oxide as a buffer layer between the ITO and the CuPcs improved the device until a PCE of 16.85% and better moisture stability [25]. The unsubstituted ZnPcs was also investigated in but a lesser extent. Introduction of ZnPcs into a planar device lead to efficiencies of 16.8% [22], 17.8% [26], in meso only to 3.5% [27] and inverted planar 11.6%. Cheng et al. used ZnPcs as a hydrophobic layer between the perovskite and the hole-transporting material Spiro-OMeTAD before, resulting in devices with a PCE of 16.8% and a stability of 91% of its initial PCE after 2400 h [28]. However, the structure of MPcs can be modified at will easily. Structural modifications of the Pcs macrocyclic ligand in the peripheral and non-peripheral positions and the choice of the core metal cation can tune essential properties like the electronic and optical properties and its solubility, which will later influence the final device performance [29]. Different strategies have been followed in the literature to improve the intrinsic low solubility of MPcs, in particular the incorporation of alkyl- [30], thiophene- [31], or arylamine (triphenylamine) groups [32], among others, at various positions [33,34]. On the other hand, the presence of Pcs substituents can be used to influence the self-assembly behavior of MPcs through the modulation of π−π intermolecular interactions between Pcs rings [35], with possible consequences on intermolecular charge transport processes [29].

Arylamine groups, in particular triphenylamine (TPA) or diphenylamine (DPA) derivatives, have been widely employed as components of small molecule-based HTMs due to their excellent hole-transporting properties, electron-donor ability, high stability, and solubility [36]. In the case of Pcs-based HTMs, molecular structure modifications by the insertion of arylamine substituents have been much less explored. In 2016, we demonstrated the use of doped DPA-tetrasubstituted ZnPcs as HTMs in PSCs, with a PCE of 11.75%. Two other ZnPcs bearing carbazole derivatives as substituents were also investigated, shedding some light on the impact of steric effects and aggregation of Pc derivatives on their charge-transport properties [37]. Later on, we reported the synthesis of Zn(II) and Cu(II)-based phthalocyanines with eight secondary aromatic amines directly linked to the peripheral positions of the macrocycle by C−N bond. These MPcs proved to be promising HTMs in PSCs, allowing PCEs ranging from 4.93% to 18.10% [38]. Sfyri et al. also implemented a ZnPcs bearing four peripheral TPA substituents in PSCs, and its use as HTM led to device efficiencies of 5.6% [39]. In another recent example, Feng et al. compared the photovoltaic performance of PSCs fabricated with OMe-DPA-CuPcs and OMe-TPA-CuPcs, featuring four bis-(4-methoxyphenyl)amino substituents and four *N, N*-bis(4-methoxyphenyl)benzenamino substituents, respectively. OMe-DPA-CuPcs showed a lower PCE than OMe-TPA-CuPcs (16.73% vs. 19.67%). This fact was ascribed to the lower HOMO energy level of OMe-TPA-CuPcs and its lower recombination rate and more efficient hole transport properties [40]. The limited data shows that arylamine-substituted MPcs have a great potential as HTMs in PSCs, which can be fully unleashed through the rational design of novel compounds of this class.

Alkyl side chains in organic semiconductors are insulating units and do not directly contribute to charge transport in organic electronic devices. Nevertheless, alkyl side-chains can have a noticeable impact on charge transport for polymer and small molecule semiconductors, including MPcs, by influencing intermolecular interactions and/or film morphology in solid-state due to two competing effects: steric hindrance and intermolecular dispersive attraction [41]. Therefore, even subtle alterations on chain length, branching position, odd-even effect, and stereochemistry of alkyl chains can significantly affect charge mobility [30]. Thus, L. Calió et al. reported the use of two MPcs (M = Cu(II) or Zn(II)) with 4-*tert*-octylphenoxy substituents as HTMs in PSCs, achieving PCEs of 8.33% and 7.25% for the Cu(II) and the Zn(II) complex, respectively [42]. More importantly, we could prove that MPcs featuring bis(4-alkoxyphenyl)amino substituents were superior HTMs with respect to their 9*H*-carbazol-9-yl and diphenylamino analogs, with subtle yet clear differences elicited by the nature of the alkoxy chains [37,38]. In that context, the best photovoltaic performance was obtained with ZnPc **BL40** (Fig. 1) bearing eight bis(4-*n*-butoxyphenyl)amino substituents. This prompted us to evaluate further the effects of the alkoxy chain length and branching on the behavior of diarylamine-substituted MPcs. To this end, we have now synthesized and tested ZnPcs complexes **Zn-BL54, Zn-BL58,** and CuPc complexes **Cu-BL57, Cu-BL61** (Fig. 1).

2. Results and discussion

2.1. Synthesis of tetrasubstituted MPcs

Metal-templated cyclotetramerization of suitable phthalonitrile precursors provides convenient access to MPcs bearing either four or eight bis(4-alkoxyphenyl)amino substituents [37,38]. However, preparing the 4,5-disubstituted phthalonitriles required to synthesize octasubstituted MPcs such as **BL40** is a rather cumbersome multi-step process. On the contrary, phthalonitriles **1** and **2**, the starting materials for the preparation of MPcs **Zn-BL54, Cu-BL57** and **Zn-BL58, Cu-BL61**, respectively, were readily obtained in excellent yields (88−93%) by Palladium-catalyzed amination reaction between 4-iodophthalonitrile and the corresponding secondary aromatic amine (Scheme 1). MPcs **Zn-BL54, Cu-BL57, Zn-BL58, Cu-BL61** were subsequently obtained as mixtures of positional isomers by cyclotetramerization reaction of these phthalonitriles in the presence of 1,8-diaza-bicyclo[5.4.0]undec-7-ene (DBU) and a metal salt (Scheme 1). Analytical data of **Zn-BL54, Cu-BL57, Zn-BL58, Cu-BL61** were in complete agreement with the proposed structures.

The new octasubstituted MPcs are soluble in common organic solvents such as THF or DCM. However, NMR characterization could not be performed on the paramagnetic CuPcs **Cu-BL57** and **Cu-BL61**. The chemical structure of these two compounds was nonetheless confirmed by UV−Vis, FTIR, and HRMS data (see experimental methods).

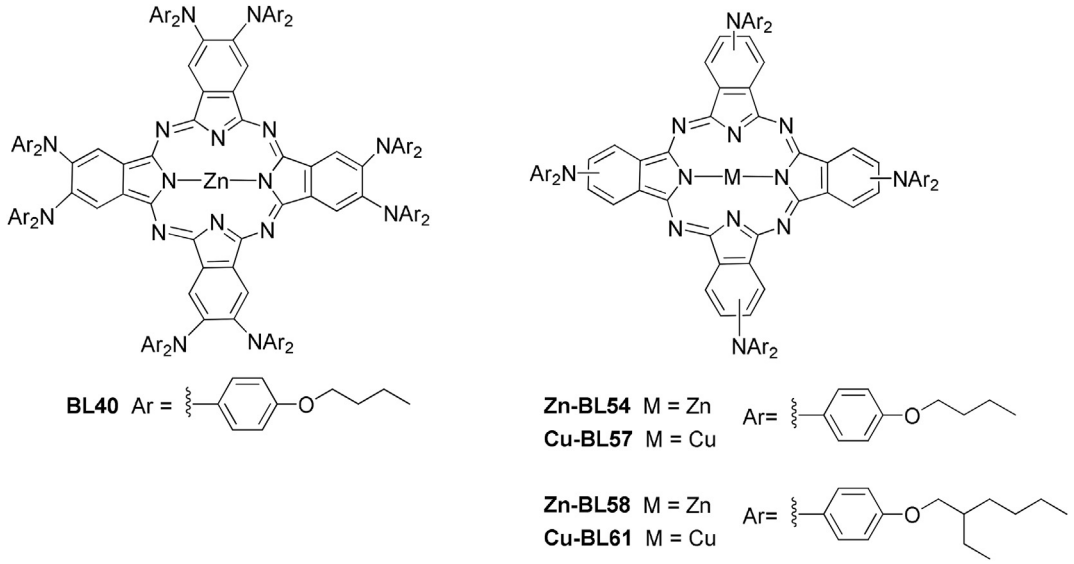

Fig. 1. Molecular structure of Zn(II) and Cu(II) phthalocyanines bearing bis(4-alkoxyphenyl)amino substituents.

2.2. Photophysical, electrochemical, and 2D GIWAXS characterization of MPcs

Typical B and Q bands of MPcs in the near UV region and Vis region, respectively, characterize the UV–Vis spectra of the new compounds (Fig. 2), which also show broad bands of low intensity in the 450–550 nm region. These bands are distinctive of MPcs with aromatic secondary amine substituents [37,38]. The energy required for the $\pi \rightarrow \pi^*$transition (a1u→eg*) from HOMO to lowest unoccupied molecular orbital (LUMO) of the Pc ring, which is responsible for the Q band, is significantly lower for most peripherally-substituted Cu- and ZnPcs tested so far as solution-processable HTMs in PSCs, including ZnPcs bearing four diaryl amino substituents without alkoxy side chains. [38] For example, a bathochromic effect in the order of +20 nm is observed for the Q bands of ZnPcs **Zn-BL54**,**58** (739 nm, THF solution) with respect to their analogue ZnPcs **BL25** (720 nm, THF solution) depleted of alkoxy side-chains [38]. An additional, although much smaller, red-shift of the absorption maxima is triggered by changing the coordinated metal species from Zn(II) to Cu(II). Thus, CuPcs **Cu-BL57** and **Cu-BL61** show absorption maxima at 744 nm and 745 nm, respectively. These data also show that the influence of branching and elongation of the alkoxy side chains on UV–Vis absorption is negligible. On the other hand, the energy required for the $\pi \rightarrow \pi^*$ transition in MPcs bearing four peripheral bis(4-alkoxyphenyl) amine substituents is higher than that required for their octa substituted analogue, as exemplified by comparison between **Zn-BL54** and **BL40** (758 nm, THF solution).

Cyclic voltammetry (CV) measurements were performed with a standard three-electrode configuration to experimentally investigate the highest occupied molecular orbital (HOMO) energy levels (E_{HOMO}) of the undoped HTM materials **Zn-BL54**, **Cu-BL57**, **Zn-BL58,** and **Cu-BL61** (Supporting Information Figure S1, Table S1). The compounds were tested in dichloromethane solution containing 0.1 M n-Bu_4NPF_6 as a supporting electrolyte, and the oxidation potential was calibrated against ferrocene used as an internal standard.

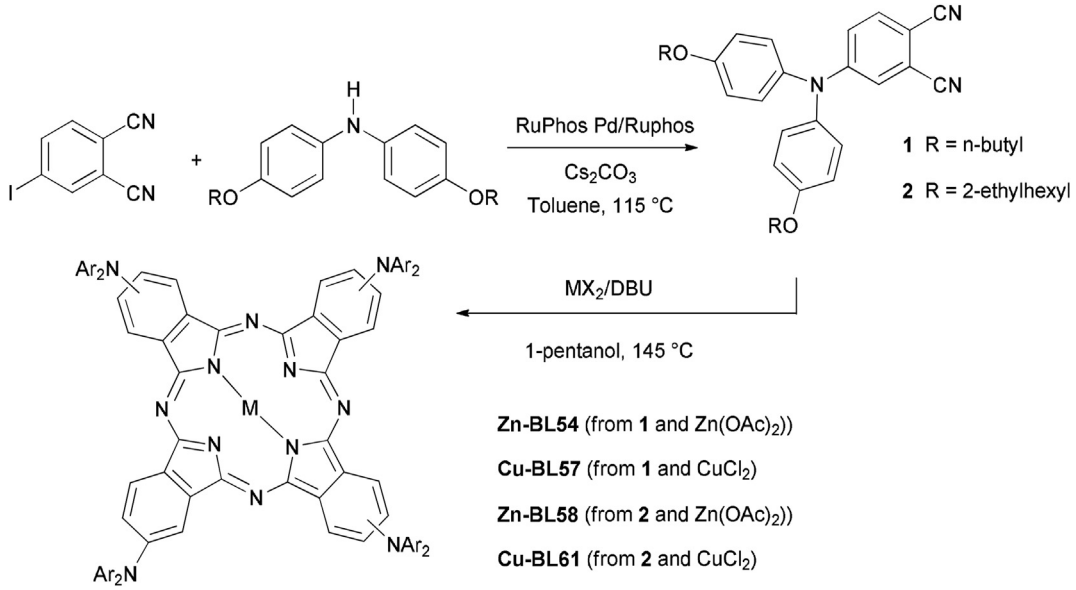

Scheme 1. Synthesis of tetrasubstituted MPcs.

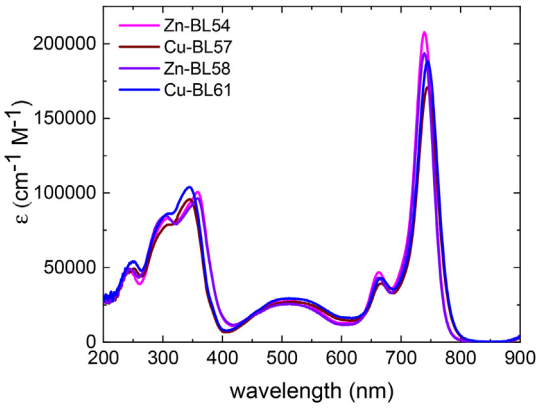

Fig. 2. UV–Vis spectra of tetrasubstituted MPcs in THF solution.

The E_{HOMO} values were calculated to be −5.37, −5.48, −5.36, and −5.46 eV *vs* vacuum for **Zn-BL54**, **Cu-BL57**, **Zn-BL58,** and **Cu-BL61**, respectively (Table S1). Slightly deeper HOMO levels were observed for Cu(II) based phthalocyanines **Cu-BL57** and **Cu-BL61** compared to Zn(II) based phthalocyanines **Zn-BL54** and **Zn-BL58**. The electron-donating effect of the longer branched alkoxy chains of **Zn-BL58** and **Cu-BL61** resulted in relatively higher HOMO levels than **Zn-BL54** and **Cu-BL57** [43].

Quantum chemical calculations were performed with the Gaussian 09W program to establish the most probable molecular geometry and energy levels in solid-state for the HTMs. The density functional theory (DFT) method B3LYP/6-311G was used for geometry optimization [44]. The optimized structures highlight the non-planar conformation of the arylamine moiety and the twists between the core nitrogen and phenyl groups (Supporting Information Figure S2a). The side-view from the optimized structure shows that the Pc core is not altered by changing the side-chains (Supporting Information Figure S2b). The electron density distributions for the highest occupied molecular orbital HOMO-1, HOMO, LUMO and LUMO+1, are presented with their corresponding energy levels (Supporting Information Figure S3). The values extracted from the DFT calculations are shown in Table S2. The bandgap (Eg) was calculated following: $E_g = E_{LUMO}\text{-}E_{HOMO}$, see Supporting Information Figure S3. The energy level for the frontier molecular orbitals for LUMO and HOMO are shown in the schematics Supporting Information Figure S4. The trend of the calculated HOMO values follows the energy levels obtained from cyclic voltammetry. $E_{HOMO,\ DFT}$ for **Zn-BL54** = −4.52, **Cu-BL57** = −4.55, **Zn-BL58** = −4.53, **Cu-BL61** = −4.54 eV.

The photogenerated hole extraction efficiency of the new HTMs was evaluated by performing steady-state PL measurements. Therefore, triple cation perovskite films were deposited on glass, and the PL spectra were recorded under wavelength excitation at 475 nm. The new HTMs were then deposited in the same ways as during the device fabrication, and the PL emission spectra were again recorded. Interestingly, a stronger quenching effect can be observed compared to the **spiro-OMeTAD** spectra (Fig. 3a). The most substantial quenching effect can be observed for **Zn-BL54** and **Cu-BL57 HTMs** (98, 99 quenching %, respectively, see Table S3), with the *n*-butoxy side chain in their structure. Less quenching can be observed for **Zn-BL58** and **Cu-BL61** (83 and 89% quenching, respectively **(**Table S3), which bear 2-ethylhexyloxy chains. This indicates that the *n*-butoxy-substituted MPcs have an enhanced hole extraction as observed in the zoom-in Fig. 3a compared to their 2-ethylhexyloxy-based Pcs counterparts. The PL quenching trend **Cu-BL57**>**Zn-BL54**>**Cu-BL61**>**Zn-BL58**>**spiro-OMeTAD** indicates the best hole-transfer between **Cu-BL57** and the perovskite [45].

The observation follows the general trend where the bulkier alkoxy groups seem less optimal for the charge transfer. Interestingly, the decrease in PL intensity suggests a good hole-extraction between the VB of the perovskite and the HOMO of the HTMs, probably due to a good perovskite/HTM interface [46]. In addition to the quenching, we also observed a red-shift in the PL_{max} for the HTMs **Zn-BL54 (**PL_{max} = 783 nm) and **Cu-BL58 (**PL_{max} = 776 nm) compared to the HTMs **Zn-BL57 (**PL_{max} = 764 nm) and **Cu-BL61 (**PL_{max} = 770 nm). To evaluate further the HTMs, time-resolved photoluminescence (TrPL) measurements were performed (Fig. 3b). Therefore, the samples were prepared in the same manner as described for the steady-state PL measurements and measured with an excitation wavelength of 640 nm. The corresponding decays were fitted to a double exponential equation, where the fast component (τ_1) is related to trap-assisted recombination at defect sites and the slow component (τ_2) to radiative recombination inside the grains (see the fitted values in Table S4). As observed, the bare perovskite film exhibits τ_1 and τ_2 values of 139 ns and 336 ns, respectively. These values decrease significantly after depositing the HTM following the trend perovskite>**Zn-BL58**>**Cu-BL61**>**Zn-BL54**>**Cu-BL57**>**spiro-OMeTAD**. This data indicates that all new HTMs exhibit a slightly slower process than **spiro-OMeTAD**, indicating slower charge recombination processes for the new HTMs than the reference containing **spiro-OMeTAD** [8]. It also indicates that the HTMs employing the less bulky alkoxy chains (**Zn-BL54** and **Cu-BL57**) extract the charges faster than those employing the more bulky alkoxy chains (**Zn-BL58** and **Cu-BL61**).

2D grazing incidence wide-angle X-ray scattering (2D GIWAXS) was performed to investigate the crystallization and the π→π stacking of the reference HTM (**spiro-OMeTAD**) and the novel HTMs with a different alkoxy group and central metal (Fig. 3c and d and Supporting Information Figure S5) [45,47]. The samples were prepared by spin-coating the corresponding HTM solutions on silicon wafers. No π–π stacking or lamella structure can be observed for the **spiro-OMeTAD** (Fig. 3c). For the four new HTMs, two diffractions rings appeared corresponding to the π–π stacking structure ($q \approx 1.4$ Å^{-1}) and the lamellar structure ($q \approx 0.3$ Å^{-1}) (Fig. 3d and Supporting Information Figure S5, S6). The lamellar structure can be more dominantly observed on the samples **Cu-BL57** and **Cu-BL61** than the samples with Zn(II) metal core (Supporting Information Figure S5). The azimuthally integrated intensity profile was calculated from 2D GIWAXS spectra (Supporting Information Figure S7). The d-spacings for the π–π stacking structure was 4.6 Å for all the HTMs, while the intercolumnar organization and distance were different for all HTMs: **Zn-BL54** = 18.9 Å, **Zn-BL58** = 22.3 Å, **Cu-BL57** = 22.3 Å, and **Cu-BL61** = 24.1 Å. Interestingly, the lamellar distance increases by exchanging Zn(II) with Cu(II) and exchanging the *n*-butoxy with 2-ethylhexyloxy side chain. The calculated angular dependence of the peak intensity at $q = 1.4$ Å^{-1} corresponds well to d-spacings of π–π stacking (4.6 Å) from the MM2 simulation (Supporting Information Figure S8). To investigate if there is a preferred crystal orientation, the set-up was the following: theta (θ) is the angle to the q_z axis (out-of-plane), whereas θ = 90° is q_{xy} axis (in-plane). Regarding the 2D GIWAXS patterns, all four HTMs show π–π stacking interaction and random orientation (Fig. 3). Since the intensity of each HTM shows no change as a function θ, all HTMs are isotropic (Fig. 3d inset and Supporting Information Figure S9). The π–π stacking peak at 1.6 Å^{-1} shows isotropic orientation, and its stacking phase is randomly arranged according to the broad peak at 0.3 Å^{-1}. Notably, the simulated molecular size of HTMs is consistent with the GIWAXS data (Supporting Information Figure S10) and confirms the trend of the lamellar size structure. At equal side chains, the HTMs incorporating Cu(II) are more significant than those incorporating Zn(II).

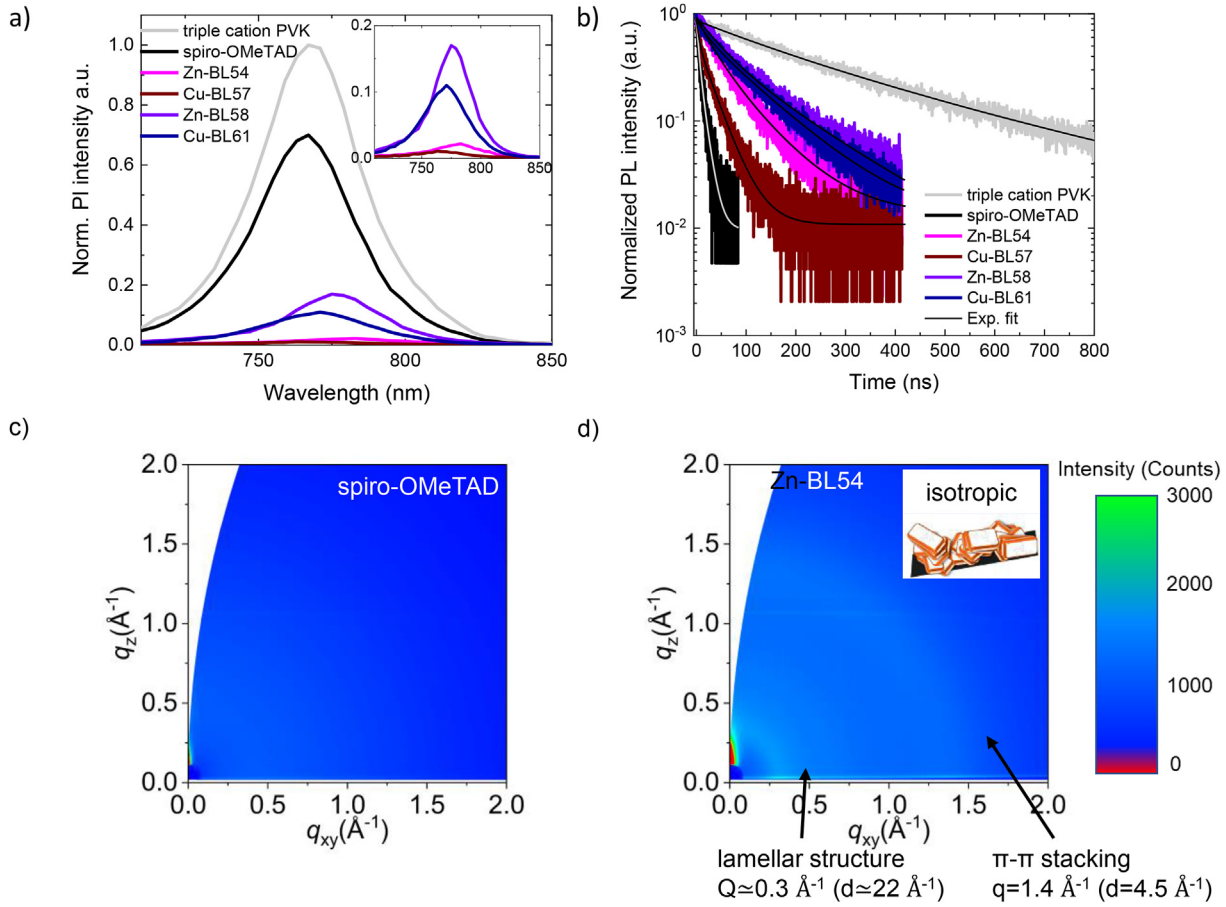

Fig. 3. a) Steady-state photoluminescence spectra (λ_{exc} = 475 nm), b) time-resolved PL decay (λ_{exc} = 640 nm, λ_{em} = 760 nm). GIWAXS pattern of the films coated on a silicon wafer: c) **spiro-OMeTAD** and d) **Zn-BL54.**

2.3. Photovoltaic performance of solution-processed PSCs

The new octasubstituted MPcs were evaluated as doped-HTMs in *n-i-p* PSCs. Solar cell devices were fabricated with the following device layout: FTO/c-TiO_2/m-TiO_2/SnO_2/perovskite/HTM/Au. All layers were deposited by solution process except for the thermally-evaporated gold electrode. The 'so-called' triple cation perovskite $[(FAPbI_3)_{0.87}(MAPbBr_3)_{0.13}]_{0.92}(CsPbI_3)_{0.08}$ was used for initial screening as a light absorber. **Spiro-OMeTAD** and octasubstituted MPcs HTM layers were doped with cobalt (III)- tris(bis-(trifluoromethylsulfonyl)imide) (CoTFSI) and (trifluoromethylsulfonyl) imide lithium salt (LiTFSI). To increase the LiTFSI solubility and the HTM thin film morphology *tert*-butylpyridine (TBP) was added to the HTM solution [48]. Top-view and cross-section scanning electron microscopy (SEM) were performed to determine the morphology and thickness of the HTMs (Fig. S11). The cross-section images show a compact and uniform hole-transporting layer with a thickness of ~247 nm for **spiro-OMeTAD**-based devices and a thickness of ~170 nm hole transporting layer for devices containing **Zn-BL54**, **Cu-BL57,** and **Zn-BL58** and **Cu-BL61**, respectively. The top-view images show complete and homogeneous coverage of the perovskite by the HTM without aggregating the material and/or pinholes (Supporting Information Figure S11).

Fig. 4a displays a schematic of the energy level diagram of the fabricated devices. The solid-state ionization potential (IP) of the doped HTMs was extracted from He I (21.22eV) ultraviolet photoelectron spectroscopy (UPS) measurements (Supporting Information Figure S12). In brief, thin films of the doped HTMs were spin-coated according to the conditions mentioned in the Experimental section (device fabrication part). The work function (WF) and the energy cut-off onset values were obtained via a linear fit at the secondary electron cut off and the HOMO onset from VB spectra, respectively (see Fig. S12 and Table S1). By adding WF and energy cut-off onset values, IP values were obtained, which represents the HOMO level of the material.

The ionization potential values of the doped HTMs layers are −5.29 eV for **spiro-OMeTAD** and −5.51, −5.61, −5.44 and −5.57 eV for **Zn-BL54**, **Cu-BL57**, **Zn-BL58** and **Cu-BL61**, respectively. The trend observed in the UPS measurement agrees with the one observed by CV. The HOMO levels align well with the valence band energy level of the typical lead iodide-based perovskites (−5.70 eV) (Supporting Information S13, Table S5).

The best-performing devices fabricated with the triple cation perovskite and the **BL**-series HTMs and **spiro-OMeTAD** are compared in Fig. 4b, and the corresponding photovoltaic parameters are extracted and displayed in Table 1. The reference device employed **spiro-OMeTAD** as HTM showed the highest efficiency with a PCE of 17.72%. **Zn-BL54** provided the best results in the BL-series with a PCE of 13.85%, followed by **Cu-BL57** (11.36%), featuring *n*-butoxy chains. The two HTMs characterized by the presence of bulkier 2-ethylhexyloxy chains, **Cu-BL61** (10.15%) and **Zn-BL58** (9.92%), provided lower PCE values than **Zn-BL54** and **Cu-BL57**. This finding indicates that the alkoxy side chains are more relevant than the coordinated metal species in determining the photovoltaic performance of these octasubstituted MPcs. The PCE trend can be

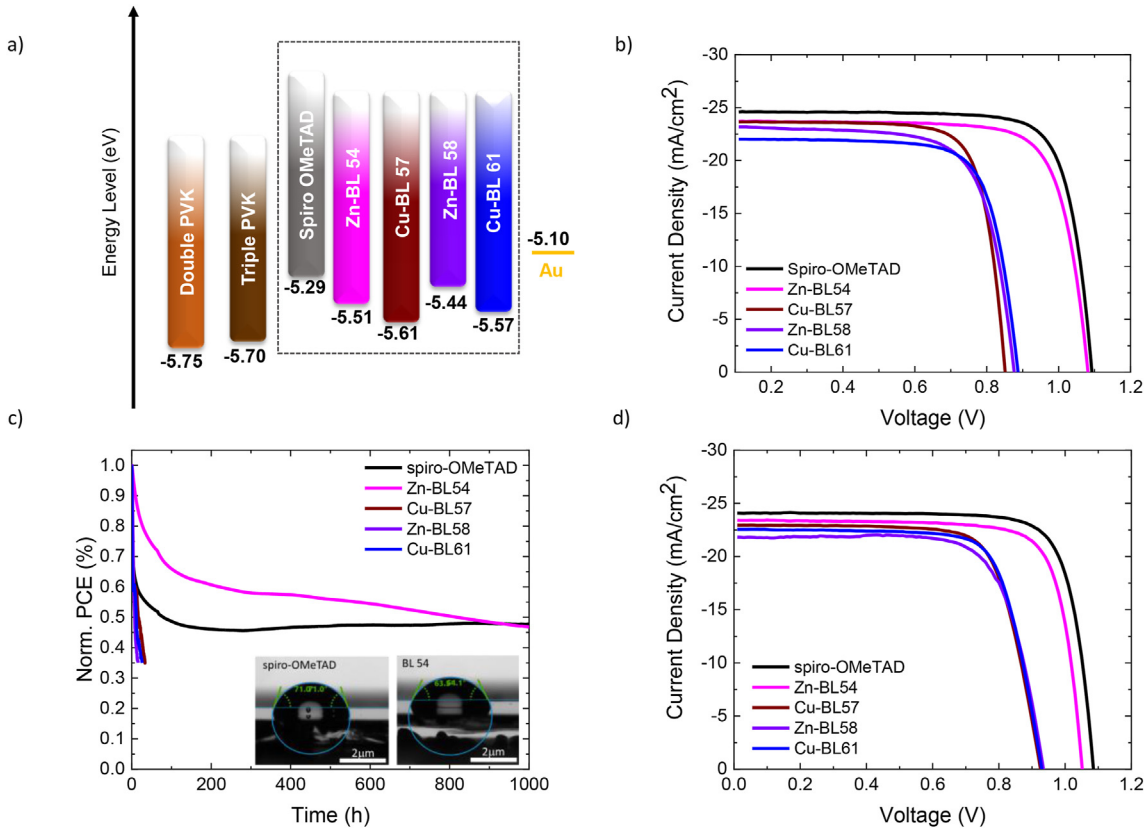

Fig. 4. a) Energy level diagram of the device containing doped HTMs (HOMO values for the HTMs, double and triple cation perovskite from their corresponding UPS measurements), b) *J–V* curves of the most efficient devices based on triple cation perovskite, c) long-term stability of unencapsulated triple cation-based devices measured under continuous light illumination at 25 °C in a nitrogen atmosphere and with inset water contact angle of **spiro-OMeTAD** and **Zn-BL54** deposited on top of the perovskite layer and d) *J–V* curves of the most efficient solar cells containing double cation-based perovskite.

related to the conductivity values obtained for the HTMs (Supporting Information Figure S14, Table S6). Indeed, the HTMs with the branched, sterically hindering 2-ethylhexyloxy chain (**Zn-BL58** = 3.22×10^{-6} cm^2/Vs and **Cu-BL61** = 7.3×10^{-6} cm^2/Vs) show lower conductivity compared to the HTMs with linear and shorter *n*-butoxy chain (**Zn-BL54** = 1.96×10^{-5} cm^2/Vs and **Cu-BL57** = 7.97×10^{-5} cm^2/Vs). It must be noted, that even though **Cu-BL57** has the highest conductivity of the **BL**-series, the efficiency is only the second best, which is indicating that also the coordination metal is playing a role. The reference HTM **spiro-OMeTAD** shows the highest conductivity with 3.4×10^{-4} cm^2/Vs which can be related to the highest efficiency.

A deeper analysis of the photovoltaic characteristics for the triple cation perovskite devices can be found in Table 1. **Zn-BL54** and **Cu-BL57** have different short-circuit current densities (J_{sc}) values, ranging from −23.73 mA/cm^2 for **Zn-BL54** to −23.66 mA/cm^2 for **Cu-BL57**. Substitution of the *n*-butoxy chains present in these two MPcs with 2-ethylhexyloxy chains leads to lower J_{sc} values for **Zn-BL68** (J_{sc} = −23.19 mA/cm^2) and **Cu-BL61** (J_{sc} = −22.02 mA/cm^2). Both factors, the kind of alkoxy chain and coordinated metal, seem to play a role here.

Table 1
Photovoltaic parameters extracted from the corresponding *J–V* curves for triple cation and double cation-based most efficient devices.

Perovskite	HTM	J_{sc} (mA/cm^2)	V_{oc} (V)	FF	PCE (%)
Triple cation	**spiro-OMeTAD**	−24.63	1.092	0.80	21.51
	Zn-BL54	−23.73	1.081	0.78	20.00
	Cu-BL57	−23.66	0.850	0.78	15.68
	Zn-BL58	−23.19	0.880	0.73	14.89
	Cu-BL61	−22.02	0.886	0.76	14.82
Double cation	**spiro-OMeTAD**	−24.86	1.09	0.79	21.30
	Zn-BL54	−23.87	1.07	0.79	20.18
	Cu-BL57	−23.00	0.94	0.74	16.00
	Zn-BL58	−22.12	0.95	0.73	15.34
	Cu-BL61	−22.57	0.94	0.75	15.91

The fill factor (FF) values for **Zn-BL58** and **Cu-BL61**, the HTMs with 2-ethylhexyloxy side chains, are lower than those measured for **Zn-BL54** and **Cu-BL57**. This trend in FF can be related to the enhanced conductivity of MPcs with *n*-butoxy chains (**Zn-BL54** and **Cu-BL57)** discussed before. When comparing further the parameters of device performance of the **BL** series to **spiro-OMeTAD**, then another main parameter leading to lower performance is the open-circuit voltage (V_{oc}). The best performing cell with **spiro-OMeTAD** has a V_{oc} value of 1.09 V, while the cells containing the BL HTM series **Zn-BL54**, **Cu-BL57**, **Zn-BL58,** and **Cu-BL61** exhibit lower V_{oc} values (1.08, 0.85, 0.88, 0.89 V, respectively). Changes in V_{oc} can be attributed to differences in the energy alignment between perovskite conduction band and the octasubstituted MPcs LUMO levels inducing recombination at the interface. The ionization potential values for the thin films of the new HTMs (−5.51, −5.61, −5.44, and −5.57 eV for **Zn-BL54**, **Cu-BL57**, **Zn-BL58,** and **Cu-BL61**, respectively) are suitable for perovskite energy matching, but to a lower degree in comparison to **spiro-OMeTAD** (−5.29 eV. See Supporting Information Table S1). Higher energy levels of the HTMs could prevent V_{oc} losses would be preferable for a better charge extraction [49]. The forward and reverse scan was used to calculate the hysteresis index for the triple cation devices (Supporting Information Table S7).

Finally, the long-term stability of the non-encapsulated devices with triple cation perovskite was measured under 1 sun illumination and in an N_2 atmosphere. The device lifetime was evaluated based on the 80% retention of its initial photovoltaic performance (Fig. 4c and Supporting Information Figure S15). Interestingly, the nature of the alkoxy chains affects the device performance and displays a strong influence on long-term device stability. In the **BL**-series, the presence of 2-ethylhexyloxy chains (**Zn-BL58** and **Cu-BL61**) deteriorated the long-term stability, while the device based on **Zn-BL54** presents the highest long-term stability under light illumination; such behavior suggests that the degradation of the layer is enhanced with bulkier insulating chains. On the other hand, the device based on **Cu-BL57,** the Cu(II) analogue of **Zn-BL54**, displayed much lower stability, thus pointing out a negative effect of Cu(II) coordination. Additionally, for the first 700 h, **Zn-BL54** showed outstanding good light stability compared with the most widely used HTM in PSC, **spiro-OMeTAD**, whose efficiency is reduced to 45% from its initial performance after 1000 h under constant light illumination. **Zn-BL54** is more stable until it reached 80% of its initial efficiency after 20 h, which from that point slowly decreased until 45% of its efficiency at 1000 h.

Water contact angle measurements were performed on top of glass/perovskite/doped HTMs to investigate the hydrophobicity of the HTMs (Fig. 4c, Supporting Information Figure S16). The following trend could be observed: **Zn-BL54**<**Cu-BL57**<**spiro-OMeTAD**<**Zn-BL58**<**Cu-BL61**, with contact angles of 63°, 69°, 71°, 72°, and 81° respectively. **Cu-BL61** showed a significantly higher hydrophobicity than all the other HTMs, agreeing with the presence of coordinated Cu (II) and lipophilic 2-ethylhexyloxy chains in its structure. MPcs with branched, bulkier alkoxy chains displayed a higher hydrophobic nature concerning those bearing *n*-butoxy chains, but this did not translate in improved device stability, as expected based on increased repelling moisture during the operation [50]. Quite surprisingly, despite its pretty average hydrophobicity, **Zn-BL54** ensured superior device stability among the HTMs examined, resulting from a combination of factors besides water repellency. The results so far show that the combination of Zn(II) with a shorter alkoxy chain is more beneficial when considering the device's performance.

To improve the efficiency further, we have evaluated the doped octasubstituted MPcs HTMs in perovskite solar cells containing a different perovskite composition. The double cation perovskite (FAMAPb(IBr)) was integrated into the following device structure: FTO/c-TiO_2/SnO_2/PCBM/perovskite/HTM/Au. The solid-state ionization potential of the double cation perovskite layer was extracted from UPS measurements. The work function, the energy-cut off, and the ionization potential are presented in Supporting Figure S17 and Table S8. It can be observed that the energy level of the double cation perovskite is −5.75 eV, slightly deeper than the triple cation perovskite. The *J*–*V* curves for the best performing device with double cation perovskite are shown in Fig. 4d. The corresponding device parameters necessary for a deeper analysis of the photovoltaic parameters are shown in Table 1 and the hysteresis index is displayed in the Supporting Information Table S9. The same efficiency trend can be observed for double cation than for triple cation perovskite (see Fig. 4d, Table 1). The reference device employed **spiro-OMeTAD** as HTM showed the highest efficiency with a PCE of 21.30%. **Zn-BL54** provided the best results in the **BL**-series with a PCE of 20.18%, followed by **Cu-BL57** (16.00%), both featuring *n*-butoxy chains. The two HTMs characterized by the presence of bulkier 2-ethylhexyloxy chains, **Cu-BL61** (15.91%) and **Zn-BL58** (15.34%), provided lower PCE values than **Zn-BL54** and **Cu-BL57**.

The J_{sc} value for the double cation devices is higher than triple cation devices. This might be due to the better crystallization of the perovskite, influenced positively by adding MACl into the solution [51]. Several reports stated before that the addition of MACl into the perovskite solution, leads to a better morphology and crystallinity resulting in better photophysical properties leading to higher efficiency [51–53].

However, the same trend for the J_{sc} values is observed with the triple cation perovskite devices. The exchange of the coordination metal Zn(II) to Cu(II) reduces the J_{sc}, and the addition of longer alkoxy chains reduces the J_{sc} even further. The J_{sc} is the highest for **Zn-BL54** (−23.87 mA/cm^2), followed by **Cu-BL57** (−23.00 mA/cm^2). The substitution of the *n*-butoxy with 2-ethylhexyloxy chains leads to lower J_{sc} values for **Zn-BL68** (J_{sc} = −22.12 mA/cm^2) and **Cu-BL61** (J_{sc} = −22.57 mA/cm^2). The reference cell containing **spiro-OMeTAD** exhibits a V_{oc} value of 1.09 V, the highest one, while the cells containing the BL HTM series **Zn-BL54**, **Cu-BL57**, **Zn-BL58,** and **Cu-BL61** exhibit lower V_{oc} values (1.07, 0.94, 0.95 and 0.94 V, respectively). The small changes observed in V_{oc} values between the different HTMs can be attributed to differences in the energy alignment between perovskite and the HTM.

The influence of the MPcs at the rear part of the device is again observed in the corresponding EQE spectra (Supporting Information Figure S18). The influence of the MPc at the rear part of the device is observed in the corresponding external quantum efficiency (EQE) spectra (Supporting Information Figure S18). The integrated current densities values are in good agreement (5% deviation) with the measured values from *J*-*V* characteristics. At high energy wavelengths, the EQE observed is very similar for all HTMs, staying close to 90%. Nevertheless, above 600 nm, a substantial decrease in the EQE can be observed for all HTMs of the **BL**-series, in agreement with the strong absorption band of the octasubstituted MPcs from 450 nm to 790 nm, which can be appreciated in the absorbance spectra of doped **BL**-HTM thin films from 400 nm to 800 nm (Supporting Information Figure S19). This absorption can considerably reduce the fraction of current generated by the second pass of reflected light from the gold electrode. As the perovskite film exhibits a higher absorption coefficient at a shorter wavelength, this effect can only be observed for low-energy photons. Compared to the reference cell with **spiro-OMeTAD**, which is transparent in the visible range, octasubstituted MPcs absorb part of this light, causing a decrease in the incident photon-to-current conversion efficiency above 590 nm [54].

Finally, the long-term stability of the non-encapsulated devices with double cation perovskite was measured under 1 sun illumination and in an N_2 atmosphere at maximum-power point (MPPT) tracking (Supporting Information Figure S20). The device lifetime was evaluated based on the 80% retention of its initial photovoltaic performance. In the **BL**-series, the presence of 2-ethylhexyloxy chains combined with the Zn(II) coordination (Zn-BL58) deteriorated the long-term stability, while the device based on **Cu-BL61** presents the highest long-term stability under light illumination. On the other hand, the devices based on the shorter alkoxy-chain **Zn-BL54 and Cu-BL57**, displayed much lower stability than Cu-BL61, thus pointing out a negative effect of the shorter alkoxy sider-chain when applied on double-cation perovskite. Additionally, for the first 850 h, **Cu-BL61** showed outstanding good light stability (85%) compared with the most widely used HTM in PSC, **Spiro-OMeTAD**, whose efficiency is reduced to 40% from its initial performance after 850 h under constant light illumination. At 1400 h Cu-BL61 is still maintaining 75% of its initial stability.

Additionally to the substantial increase in performance, we observe higher stability for the double cation devices compared to

the triple cation ones (see the comparison on the Supporting Information Figure S20). To further enhance the whole device performance in terms of efficiency and stability, special attention must be paid to both materials, perovskite composition and MPcs HTM.

3. Conclusion

In summary, we have reported four new metal phthalocyanines, incorporating either Zn(II) or Cu(II) with *n*-butoxy or 2-ethylhexyloxy side chains used as HTMs in perovskite solar cells. Surprisingly, we found that the coordinated transition metal cation is not only driving the differences in device performance. Still, the steric hindrance of the alkoxy side chain is the factor that primarily determines the properties of the HTMs and the device performance. Our result demonstrates that the nature of the alkoxy side chains influences the molecular packing of the HTMs, which results in direct consequences in the charge carrier transport and charge recombination at the interface. Two device architectures were tested, and their advantages and disadvantages were evaluated. A more stable device could be obtained using a double cation perovskite, maintaining 80% of its original PCE until 850 h of illumination but reaching only 15.91% PCE in the case of **Cu-BL61**. A much higher PCE of 20.18% could be reached using the best performing HTM **Zn-BL54.**

4. Experimental section

4.1. Synthesis of metallophthalocyanines

4.1.1. Materials and methods

Commercially available reagents were used as received. Bis(4-*n*-butoxyphenyl)amine and bis(4-[(2-ethylhexyl)oxy]phenyl)amine were synthesized as previously reported in the literature [55,56]. Solvents were purified by standard methods and dried if necessary. Reactions were monitored by thin-layer chromatography (TLC) conducted on plates precoated with silica gel Si 60-F254 (Merck, Germany). Column chromatography was conducted using silica gel Si 60, 0.063–0.200 mm (normal) or 0.040–0.063 mm (flash) (Merck, Darmstadt, Germany). Melting points were determined with a capillary melting point apparatus Büchi B-540. UV–Vis measurements in solution were performed on a Nicolet Evolution 500 spectrophotometer (Thermo Electron Corporation). FTIR was performed on a Cary 530 instrument (Agilent Technologies). ^{1}H NMR and ^{13}C NMR spectra were recorded on a Bruker Avance 400 spectrometer; chemical shifts are indicated in parts per million downfield from $SiMe_4$, using the residual proton ($CHCl_3$ = 7.26 ppm, CH_2Cl_2 = 5.32 ppm, Pyridine = 7.22 ppm) and carbon ($CDCl_3$ = 77.0 ppm, CD_2Cl_2 = 54.0 ppm) solvent resonances as the internal reference. Coupling constant values *J* are given in Hz.

4.1.2. 4-[Bis(4-*n*-butoxyphenyl)amino]phthalonitrile ***1***

A flame dried Schlenk tube equipped with a stir bar was charged with 4-iodophthalonitrile (560 mg, 2.2 mmol), bis(4-*n*-butoxyphenyl)amine (627 mg, 2.0 mmol), Ruphos (9 mg, 0.02 mmol) and Ruphos Pd (17 mg, 0.02 mmol). The Schlenk tube was evacuated and backfilled with nitrogen three times. Degassed toluene (4 mL) and dry Cs_2CO_3 (715 mg, 2.2 mmol) were added, and the reactor was brought into an oil bath preheated at 115 °C. The reaction mixture was stirred at this temperature for 16 h. After cooling to room temperature, the mixture was diluted with CH_2Cl_2 and filtered on Celite. The solvent was evaporated under reduced pressure. The residue was purified by flash column chromatography (silica gel, hexane/EtOAc 85/15) to give the title compound a thick oil that slowly solidifies on standing (408 mg, 93%). Mp 145–147 °C. ^{1}H NMR (400 MHz, CD_2Cl_2) δ 7.43 (d, *J* = 8.9 Hz, 1H), 7.19–7.12 (m, 4H), 7.04 (d, *J* = 2.5 Hz, 1H), 6.97–6.92 (m, 5H), 3.98 (t, *J* = 6.5 Hz, 4H), 1.83–1.73 (m, 4H), 1.58–1.45 (m, 4H), 0.99 (t, *J* = 7.4 Hz, 6H). ^{13}C NMR (101 MHz, CD_2Cl_2) δ 158.42, 152.87, 137.37, 134.68, 128.72, 120.31, 119.37, 117.34, 116.97, 116.63, 116.48, 102.71, 68.56, 31.77, 19.74, 14.17.

4.1.3. 4-[Bis(4-[(2-ethylhexyl)oxy)phenyl]amino]phthalonitrile ***2***

Palladium-catalyzed amination of 4-iodophthalonitrile (560 mg, 2.2 mmol) with bis(4-[(2-ethylhexyl)oxy]phenyl)amine (851 mg, 2.0 mmol) was performed as described for phthalonitrile **1**. Flash column chromatography (petroleum ether/EtOAc 93/7) gave the title compound as a thick oil that slowly solidifies on standing (970 mg, 88%). Mp 48–51 °C. ^{1}H NMR (400 MHz, $CDCl_3$) δ 7.41 (d, *J* = 8.9 Hz, 1H), 7.10 (d, *J* = 8.7 Hz, 4H), 7.01 (d, *J* = 2.2 Hz, 1H), 6.94–6.90 (m, 5H), 3.84 (d, *J* = 5.6 Hz, 4H), 1.79–1.75 (m, 2H), 1.54–1.24 (m, 16H), 0.92 (m, 12H). ^{13}C NMR (101 MHz, $CDCl_3$) δ 158.20, 152.45, 136.89, 134.37, 128.16, 120.23, 119.11, 116.85, 116.76, 116.20, 116.11, 102.53, 70.90, 39.51, 30.65, 29.22, 23.98, 23.17, 14.22, 11.26.

4.1.4. Zinc phthalocyanine ***Zn-BL54***

In a flame dried Schlenk tube, phthalonitrile **1** (439 mg, 1.0 mmol) and $Zn(OAc)_2.2H_2O$ (55 mg, 0.25 mmol) were suspended in 1-pentanol (3 mL). The mixture was stirred for 15 min under a nitrogen atmosphere, then DBU (150 μL, 1 mmol) was added, and the mixture was heated at 145 °C for a further 24 h. After cooling to room temperature, the reaction mixture was poured into MeOH, and the insoluble ZnPc was collected by filtration on a Büchner funnel. The crude compound was thoroughly washed with MeOH and dried under reduced pressure. Subsequent purification was achieved by column chromatography (silica gel, THF/hexane 4/1). The isolated ZnPc was then dissolved in DCM (30 mL) and reprecipitated by adding MeOH (15 mL). The title compound was obtained as a mixture of positional isomers (298 mg, 65%). UV–Vis (THF): λ_{max}/nm (log ε) = 358 (5.01), 514 (4.44), 663 (4.67), 739 (5.32). FTIR (KBr): υ_{max}/cm^{-1} = 3060, 3035, 2958, 2923, 2871, 1727, 1605, 1506, 1470, 1402, 1384, 1338, 1240, 1172, 1126, 1096, 1055, 827, 762. ^{1}H NMR (400 MHz, Pyridine-d5, 80 °C) δ 9.58–9.36 (m, 4H), 9.25–9.13 (m, 1H), 8.02–7.71 (m, 4H), 7.61–7.44 (m. 20H), 7.24–7.13 (m, 20H), 4.14–4.05 (m, 16H), 1.93–1.79 (m, 16H), 1.67–1.51 (m, 16H), 1.05–0.95 (m, 24H). HRMS (MALDI-TOF): *m/z* calcd for $(C_{112}H_{116}N_{12}O_8Zn)^+$ 1820.833. Found: 1820.815.

4.1.5. Copper phthalocyanine ***Cu-BL57***

In a flame dried Schlenk tube, phthalonitrile **1** (439 mg, 1.0 mmol) and $CuCl_2$ (34 mg, 0.25 mmol) were suspended in 1-pentanol (3 mL). The mixture was stirred for 15 min under a nitrogen atmosphere, then DBU (150 μL, 1 mmol) was added, and the mixture was heated at 145 °C for a further 24 h. After cooling to room temperature, the reaction mixture was poured into MeOH, and the insoluble CuPcs was collected by filtration on a Büchner funnel. The solid was thoroughly washed with MeOH and dried under reduced pressure. Subsequent purification of the crude product was achieved by column chromatography (silica gel, DCM). The isolated CuPcs was then dissolved in DCM (10 mL) and reprecipitated by adding MeOH (20 mL). The title compound was obtained as a mixture of positional isomers (265 mg, 58%). UV–Vis (THF): λ_{max}/nm (log ε) = 345 (4.97), 512 (4.43), 668 (4.59), 744 (5.25). FTIR (KBr): υ_{max}/cm^{-1} = 3060, 3035, 2959, 2926, 2870, 1727, 1607, 1505, 1471, 1403, 1384, 1338, 1239, 1172, 1127, 1095, 1055, 825, 759. HRMS (MALDI-TOF): *m/z* calcd for $(C_{112}H_{116}N_{12}O_8Cu)^+$ 1819.834. Found: 1819.822.

*4.1.6. Zinc phthalocyanine **Zn-BL58***

Zn(II)-templated cyclotetramerization of phthalonitrile **2** (551 mg, 1.0 mmol) was performed as described for **Zn-BL54**. The crude product was purified by column chromatography (silica gel, THF/hexane 1/1). The isolated ZnPcs was then dissolved in DCM (12 mL) and reprecipitated by the addition of MeOH (20 mL). The title compound was obtained as a mixture of positional isomers (317 mg, 56%). UV–Vis (THF): λ_{max}/nm (log ε) = 359 (4.98), 515 (441), 663 (4.63), 739 (5.28). FTIR (KBr): υ_{max}/cm^{-1} = 3060, 3035, 2957, 2926, 2859, 1725, 1604, 1505, 1468, 1384, 1333, 1238, 1169, 1127, 1086, 1045, 825, 758. ^{1}H NMR (400 MHz, Pyridine-d5) 9.63–9.36 (m, 4H), 9.24–9.07 (m, 4H), 8.02–7.70 (m, 4H), 7.65–7.45 (m, 20H), 7.28–7.17 (m, 20H), 4.05–3.92 (m, 16H), 1.89–1.24 (m, 72H), 1.08–0.78 (m, 48H). HRMS (MALDI-TOF): *m*/*z* calcd for $(C_{136}H_{165}N_{12}O_8Zn)^+$ 2158.217. Found: 2158.211.

*4.1.7. Copper phthalocyanine **Cu-BL61***

Cu(II)-templated cyclotetramerization of phthalonitrile **2** (551 mg, 1.0 mmol) was performed as described for **Cu-BL57**. The crude product was purified by column chromatography (silica gel, DCM/Hexane 3/2). The isolated CuPcs was then dissolved in DCM (15 mL) and reprecipitated by the addition of MeOH (30 mL). The title compound was obtained as a mixture of positional isomers (300 mg, 53%). UV–Vis (THF): λ_{max}/nm (log ε) = 345 (5.02), 507 (4.46), 665 (4.63), 745 (5.27). FTIR (KBr): υ_{max}/cm^{-1} = 3059, 3037, 2957, 2926, 2859, 1727, 1607, 1505, 1468, 1403, 1385, 1338, 1239, 1172, 1130, 1095, 1034, 891, 824, 760. HRMS (MALDI-TOF): *m*/*z* calcd for $(C_{136}H_{165}N_{12}O_8Cu)^+$ 2157,217. Found: 2157.236.

Voltammograms of HTMs were measured in a 0.1 M *n*-Bu_4NPF_6/DCM solution, with glassy carbon working electrode, Pt wire reference, counter electrodes, ferrocene/ferrocenium (Fc/Fc^+) as internal standard. Potentials were converted to the normal hydrogen electrode (NHE) by adding +0.64 V and −4.44 eV.

4.1.8. Perovskite thin-film and solar cell fabrication for triple cation perovskite

Laser scribed fluorine-doped tin oxide (FTO) coated glass substrates were cleaned with 2% Hellmanex solution, water, deionized water, and isopropanol in an ultrasonic bath for 5 min each and 30 min of UV/O_3 treatment. Titanium diisopropoxide bis(acetylacetonate) (TAA) (Sigma Aldrich) in isopropanol solution (1:15 v/v) was deposited by spray pyrolysis, forming after annealing at 450 °C for 30 min a 30 nm thick compact TiO_2 layer. From a TiO_2 paste (Dyesol 30 NR-D) solution (1 gr. in 9 mL ethanol dilution), a mesoporous TiO_2 (*m*-TiO_2) was prepared by spin-coating 45 μL at 5000 rpm (1000 rpm/s acceleration, 20 s). Sintering at a hot plate at 500 °C for 20 min followed. Then, a 20 nm SnO_2 was prepared dissolving $SnCl_4$ (Acros) in deionized water (12 μL in 988 μL water). This solution was spin-coated at 3000 rpm for 30 s (1000 rpm/s acceleration) on top of the meso TiO_2. After annealing at 190 °C for 1 h a 20 nm thick layer was formed. For the triple cation perovskite solution 17.41 mg MABr, 27.02 mg CsI, 57.06 mg $PbBr_2$, 178.94 mg FAI and 548.60 mg PbI_2 and it was dissolved in 1 mL of DMF:DMSO (0.78:0.22 v/v) to obtain the following composition $[(FAPbI_3)_{0.87}(MAPbBr_3)_{0.13}]_{0.92}(CsPbI_3)_{0.08}$. The solution was spin-coated for the first step at 2000 rpm for 10 s, followed by 5000 rpm for 30 s. The antisolvent chlorobenzene (100 μL) was dropped during the second step at 15 s before finishing. Annealing the films at 100 °C for 1 h followed. After cooling of the samples the HTM was spin-coated on top of the samples in the same ways as described below.

4.1.9. Materials for device fabrications for double cation perovskite

Titanium diisopropoxide bis(acetylacetonate) (TAA), 4-tert-butylpyridine (TBP), tin(IV) chloride pentahydrate, bis(trifluoromethane) sulfonamide lithium salt, and FK209 [tris(2-(1H-pyrazol-1-yl)-4-tert-butylpyridine)-cobalt(III) tris(bis(trifluoromet-hylsulfonyl) imide)], chlorobenzene (CB), dimethylsulphoxide (DMSO), dimethylformamide (DMF) were supplied from Sigma-Aldrich. FAI, MAI and $PbBr_2$ were purchased from GreatCell Solar. Lead iodide was purchased from Alfa Aesa. Spiro-OMeTAD was purchased from Merck. PCBM was supplied from lumintac. The SnO_2 nanoparticle was supplied from Alfa Aesar. All of the purchased chemicals were used as received without further purification.

4.1.10. Device fabrication for the double cation perovskite composition

The chemically etched FTO glass (Nippon Sheet Glass) was cleaned with detergent solution, acetone, and ethanol. For the compact TiO_2 (*c*-TiO_2) layer, TAA solution in ethanol (0.2 mL of TAA in 6 mL of anhydrous ethanol) was sprayed at 450 °C. SnO_2 nanoparticle were diluted in deionized water with a ratio of 1:4 and spin-coated on the *c*-TiO_2 substrate at a speed of 3000 rpm for 20 s with a ramp-up of 2000 rpm/s. Finally the samples were heated at 150 °C for 10 min. The PCBM layer was dissolved in chlorobenzene at a concentration of 10 mg/mL and spin-coated on the SnO_2 layer at a speed of 3000 rpm for 20 s with a ramp-up of 2000 rpm/s. Finally the samples were heated at 100 °C for 10 min. Afterward the perovskite solution (the ratio of PbI_2, MAI, FAI, $PbBr_2$ is 1:0.16:0.84:0.11) was spin-coated. The concentration of PbI_2 is 1.38 mmol/mL, the MACl is 0.305 mmol/mL which was additionally added into the perovskite solution. The solvent used for the perovskite solution is composed by DMSO and DMF with a ratio of 1:4. The layers are spin-coated on the substrates at 1000 rpm for 10 s and 5000 rpm for 30 s, respectively. 200 μL of chlorobenzene was dropped in 10 s at 5000 rpm. Then the perovskite films were annealed at 150 °C for 10 min. For Spiro-OMeTAD, The solution was prepared by dissolving 75 mg of Spiro-OMeTAD (Merck) with additives (23 μL of Li-bis(trifluoromethanesulfonyl), 10 μL of FK209 and 39 μL of 4-tert-butylpyridine) in 1 mL of chlorobenzene. The concentration of **BL**-series HTMs was 20 mM. The molar ratio of additives for **spiro-OMeTAD** and each doped BL-HTM solution was 0.5 for LiTFSI from a 1.8 M stock solution in acetonitrile, 3.3 for TBP and 0.03 for FK209 from a 0.25 M stock solution in acetonitrile. The HTM layers were formed by spin-coating the solution at 4000 rpm for 20 s and followed by the deposition of the 70 nm thick Au electrode by a thermal evaporation. All the preparative work to deposit PCBM, perovskite and Spiro-OMeTAD was done inside the glove box filled with nitrogen to minimize the influence of moisture.

5. Thin-film characterization

A Lambda 950S spectrophotometer (PerkinElmer, Inc.) was used to record the absorbance spectra. A Fluorolog TCSPC (HORIBA, Ltd.) was used to measure time-resolved photoluminescence (TRPL) and photoluminescence (PL) spectroscopy, with a picosecond laser with an excitation wavelength of 640 nm and 475 nm, respectively. 760 nm was the detection wavelength of time-resolved photoluminescence. An AXIS Nova, Kratos Analytical Ltd, UK ultraviolet photoelectron spectrometer, equipped with a He–I source ($h\nu$ = 21.22 eV) was used to measure the valence band energy, Fermi level and the work function. The Fermi level of the samples was referenced to that of Au which was in electrical contact with a sample in UPS measurements. A FEI Teneo Schottky Field Emission SEM was used for recording the scanning electron microscopy (SEM) images by an in-lens detector of at tension of 1.5 kV for top-view imaging and 1 kV for cross-section analysis. Conductivity measurements were carried out using the 2.5 μm channel (channel width 10 mm and height 40 nm) of an organic field-effect transistor (OFET, Fraunhofer IPMS) with two/contact electrical conductivity set-up. The

substrates were cleaned with 20 min oxygen plasma following the HTM deposition by spin-coating at 4000 rpm for 20s. The measurements were carried by sweeping from −10 to 10 V (source-drain voltage) at a scan rate of 1 V/s with a Keithley 2612A. The data were recorded with the KickStart software program and the conductivity was calculated from a linear fit of the *J-V* measurement and Ohm's law. Water-contact angle measurements on the top of the thin layers of the HTMs were measured using the KRUSS DSA100 optical contact angle instrument. Measurements were conducted using the sessile drop program with a 0.5 mm needle size. Drops of water at a rate of 0.01 mL/min and a volume of 12 μL were created. Substrates were prepared by spin coating 20 mM HTM solutions onto glass/perovskite layers. The image was recorded 1 s after the interaction of the water drop with the HTM layer. Two-dimensional wide-angle X-ray scattering (2D-WAXS) samples were prepared by spin-coating on silicon wafers the octasubstituted MPcs with the same solution concentration and processing method than in the device fabrication. Two-dimensional wide-angle X-ray scattering (2D-WAXS) patterns represented in reciprocal lattice space were performed at SPring-8 on beamline BL19B2. The samples were irradiated with X-ray energy of 12.39 keV (λ = 1 Å) at a fixed incident angle on the order of 0.12° through a Huber diffractometer. The 2D-WAXS patterns were measured with a two-dimensional image detector (Pilatus 300K).

6. Device characterization

The EQE was measured with the IQE200B (Oriel) without bias light. Before measuring the *J*–*V* curves a NREL-certified KG5-filtered Si-reference diode was used for light intensity calibration. Then a 2400 Keithley system with a Xe–lamp Oriel sol3A sun simulator (Newport Corporation) was used for the *J*–*V* measurements. The system was calibrated to AM1.5G standard conditions by using an Oriel 91150 V reference cell (*J*–*V* curves scan rate of 50 mV/s and 10 mV voltage step). A shadow mask with a metal aperture of 0.16 cm^2, defined the active area of the cell. All cells were measured without encapsulation at room temperature, and without antireflective light coating. A constant rate of 10 mV/s and 10 mV voltage step was applied for reversed bias after 5s under light soaking. A LED power source was used for the stability test which performed as maximum power tracking under 100 mW/cm^2. During the measurement a constant temperature of 25 °C was kept by a cooling system. Zero percent humidity was ensured through encapsulation in a measurement box which was purged with nitrogen gas.

Supporting information

Supporting information is available from the Wiley Online Library or from the author.

Authors' contribution

The work was conceptualized by Dr S. Orlandi, Dr Gianluca Pozzi and Prof. Nazeeruddin.

N. Klipfel and Jianxing Xia experimented with perovskite thin films and solar cells.

Dr S. Orlandi and Dr M. Cavazzini synthesized the hole-transporting materials. P. Čulík and I spin-coated the devices and characterized the devices. Dr H. Kanda helped measure the PL, TrPL data and helped with the analysis of the GIWAXS data, J. Xia did the DFT calculations, Prof. Dr N. Shibayama measured the GIWAXS data, Dr C. Igci helped with the CV measurements, and Dr C. Momblona helped with the conductivity measurements.

Vygintas Jankauskas, Kristijonas Genevicius, Abdullah M. Asiri, Kasparas Rakstys measured the hole-mobility and conductivity of the HTMs.

N. Klipfel, Wei Li and Dr. Gianluca Pozzi wrote the manuscript. Yi-Bing Cheng, Abdullah M. Asiri and M. K. Nazeeruddin supervised the project.

Declaration of competing interest

The authors declare that they have no known competing financial interests or personal relationships that could have appeared to influence the work reported in this paper.

Data availability

Data will be made available on request.

Acknowledgments

The authors acknowledge Prof. Raffaella Buonsanti for the use of the Fluorolog system and Prof. Hubert Girault for the use of water contact-angle measurement system. N.K. thanks the European Union's Horizon 2020 research and innovation program under the Marie Skłodowska Curie grant agreement no. 764787. P. Č. acknowledge the funding of the Swiss-European Mobility Program–Student Mobility for Studies' grant. H. K. acknowledge the support of the H2020 program for Solar-ERANET funding of the BOBTANDEM (2019–2022) N.S would like to acknowledge SPring-8 with the approval of the JASRI (proposal no. 2021A1952 and 2021B1870). C. M. and M. K. N. acknowledge the project German Research Foundation (Projekt number 424101351)-Swiss National Foundation (SNF) (200021E_186390).

Appendix A. Supplementary data

Supplementary data to this article can be found online at https://doi.org/10.1016/j.mtener.2022.101110.

References

[1] W. Hicks, NREL Research Pushes Perovskites Closer to Market Title, 2018.
[2] A. Kojima, K. Teshima, Y. Shirai, T. Miyasaka, J. Am. Chem. Soc. 131 (2009) 6050.
[3] K.P. Goetz, A.D. Taylor, Y.J. Hofstetter, Y. Vaynzof, ACS Appl. Mater. Interfaces 13 (2021) 1.
[4] M. Cai, Y. Wu, H. Chen, X. Yang, Y. Qiang, L. Han, Adv. Sci. 4 (2017).
[5] A. Binek, M.L. Petrus, N. Huber, H. Bristow, Y. Hu, T. Bein, P. Docampo, ACS Appl. Mater. Interfaces 8 (2016), 12881.
[6] M. Abuhelaiqa, N. Shibayama, X.X. Gao, H. Kanda, M.K. Nazeeruddin, ACS Appl. Energy Mater. 4 (2021) 3424.
[7] M. Abuhelaiqa, S. Paek, Y. Lee, K.T. Cho, S. Heo, E. Oveisi, A.J. Huckaba, H. Kanda, H. Kim, Y. Zhang, R. Humphry-Baker, S. Kinge, A.M. Asiri, M.K. Nazeeruddin, Energy Environ. Sci. 12 (2019) 1910.
[8] C. Igci, S. Paek, K. Rakstys, H. Kanda, N. Shibayama, V. Jankauskas, C. Roldán-Carmona, H. Kim, A.M. Asiri, M.K. Nazeeruddin, Sol. RRL 4 (2020) 1.
[9] C. Rodríguez-Seco, L. Cabau, A. Vidal-Ferran, E. Palomares, Acc. Chem. Res. 51 (2018) 869.
[10] G. Divitini, S. Cacovich, F. Matteocci, L. Cinà, A. Di Carlo, C. Ducati, Nat. Energy 1 (2016), 15012.
[11] Y. Han, S. Meyer, Y. Dkhissi, K. Weber, J.M. Pringle, U. Bach, L. Spiccia, Y.B. Cheng, J. Mater. Chem. A 3 (2015) 8139.
[12] N. Aristidou, I. Sanchez-Molina, T. Chotchuangchutchaval, M. Brown, L. Martinez, T. Rath, S.A. Haque, Angew. Chem. Int. Ed. 54 (2015) 8208.
[13] K. Wojciechowski, T. Leijtens, S. Siprova, C. Schlueter, M.T. Hörantner, J.T.W. Wang, C.Z. Li, A.K.Y. Jen, T.L. Lee, H.J. Snaith, J. Phys. Chem. Lett. 6 (2015) 2399.
[14] W. Tress, N. Marinova, T. Moehl, S.M. Zakeeruddin, M.K. Nazeeruddin, M. Grätzel, Energy Environ. Sci. 8 (2015) 995.

[15] F. Galatopoulos, A. Savva, I.T. Papadas, S.A. Choulis, APL Mater 5 (2017), 076102.
[16] A. Krishna, A.C. Grimsdale, J. Mater. Chem. A 5 (2017), 16446.
[17] J. Urieta-Mora, I. García-Benito, A. Molina-Ontoria, N. Martín, Chem. Soc. Rev. 47 (2018) 8541.
[18] L. Breloy, O. Yavuz, I. Yilmaz, Y. Yagci, D.L. Versace, Polym. Chem. 12 (2021) 4291.
[19] A.M. Schmidt, M.J.F. Calvete, Molecules 26 (2021) 1.
[20] C.V. Kumar, G. Sfyri, D. Raptis, E. Stathatos, P. Lianos, RSC Adv. 5 (2015) 3786.
[21] W. Ke, D. Zhao, C.R. Grice, A.J. Cimaroli, G. Fang, Y. Yan, J. Mater. Chem. A 3 (2015), 23888.
[22] C. Chen, H. Li, J. Jin, Y. Cheng, D. Liu, H. Song, Q. Dai, Nano Energy 32 (2017) 165.
[23] Z. Liu, B. Sun, X. Liu, J. Han, H. Ye, Y. Tu, C. Chen, T. Shi, Z. Tang, G. Liao, J. Mater. Chem. A 6 (2018) 7409.
[24] R. Chen, T. Bu, J. Li, W. Li, P. Zhou, X. Liu, Z. Ku, J. Zhong, Y. Peng, F. Huang, Y.B. Cheng, Z. Fu, ChemSusChem 11 (2018) 1467.
[25] T. Lei, H. Dong, J. Xi, Y. Niu, J. Xu, F. Yuan, B. Jiao, W. Zhang, X. Hou, Z. Wu, Chem. Commun. 54 (2018) 6177.
[26] C. Chen, Long-lasting nanophosphors applied to UV-resistant and energy storage perovskite, Adv. Energy Mater. 7 (2017) 1700758, pdf.
[27] A. Suzuki, T. Kida, T. Takagi, T. Oku, Ppn. J. Appl. Phys. 55 (2016), 02BF01.
[28] A. Ioakeimidis, C. Christodoulou, M. Lux-Steiner, K. Fostiropoulos, J. Solid State Chem. 244 (2016) 20.
[29] Y. Matsuo, K. Ogumi, Y. Matsuo, I. Jeon, T. Nakagawa, Y. Matsuo, H. Wang, K. Ogumi, RSC Adv. 10 (2020), 32678.
[30] T. Lei, J.Y. Wang, J. Pei, Chem. Mater. 26 (2014) 594.
[31] Z. Dalkılıç, C.B. Lee, H. Choi, I. Nar, N.K. Yavuz, A.K. Burat, J. Organomet. Chem. (2020), 121419.
[32] Y. Feng, Q. Hu, E. Rezaee, M. Li, Z.-X. Xu, A. Lorenzoni, F. Mercuri, M. Muccini, Adv. Energy Mater. 9 (2019), 1970104.
[33] A.A. Chernonosov, E.A. Ermilov, B. Röder, L.I. Solovyova, O.S. Fedorova, Bioinorgan. Chem. Appl. 2014 (2014).
[34] Q.D. Dao, A. Fujii, R. Tsuji, Y. Takeoka, M. Ozaki, Org. Electron. 43 (2017) 156.
[35] C. Piechocki, J. Simon, A. Skoulios, D. Guillon, P. Weber, J. Am. Chem. Soc. 104 (1982) 5245.
[36] M.M.H. Desoky, M. Bonomo, R. Buscaino, A. Fin, G. Viscardi, C. Barolo, P. Quagliotto, Energies 14 (2021) 2279.
[37] K.T. Cho, K. Rakstys, M. Cavazzini, S. Orlandi, G. Pozzi, M.K. Nazeeruddin, Nano Energy 30 (2016) 853.
[38] K.T. Cho, M. Cavazzini, K. Rakstys, S. Orlandi, S. Paek, M. Franckevičius, H. Kanda, R. Gegevičius, Q.V. Emmanuel, G. Pozzi, M.K. Nazeeruddin, ACS Appl. Energy Mater. 2 (2019) 6195.
[39] G. Sfyri, N. Vamshikrishna, C.V. Kumar, L. Giribabu, P. Lianos, Sol. Energy 140 (2016) 60.
[40] Y. Feng, Q. Hu, E. Rezaee, M. Li, Z.X. Xu, A. Lorenzoni, F. Mercuri, M. Muccini, Adv. Energy Mater. 9 (2019) 1.
[41] Z. Ma, H. Geng, D. Wang, Z. Shuai, J. Mater. Chem. C 4 (2016) 4546.
[42] L. Caliò, J. Follana-Berná, S. Kazim, M. Madsen, H.G. Rubahn, Á. Sastre-Santos, S. Ahmad, Sustain. Energy Fuels 1 (2017) 2071.
[43] Y. Chen, T. Liu, L.K. Ma, W. Xue, R. Ma, J. Zhang, C. Ma, H.K. Kim, H. Yu, F. Bai, K.S. Wong, W. Ma, H. Yan, Y. Zou, J. Mater. Chem. A 9 (2021) 7481.
[44] M.J. Frisch, G.W. Trucks, H.B. Schlegel, G.E. Scuseria, M.A. Robb, J.R. Cheeseman, J.A. Montgomery, T. Vreven, K.N. Kudin, J.C. Burant, Gaussian 09, Revision A.02, 2009. Wallingford, CT.
[45] Y. Feng, Q. Chen, L. Dong, Z. Zhang, C. Li, S. Yang, S. Cai, Z.X. Xu, Sol. Energy 184 (2019) 649.
[46] G. Xing, N. Mathews, S.S. Lim, Y.M. Lam, S. Mhaisalkar, T. C. Sum 6960 (2013) 498.
[47] Z. Dalkılıç, C.B. Lee, H. Choi, I. Nar, N.K. Yavuz, A.K. Burat, J. Organomet. Chem. (2020), 121419.
[48] S. Wang, M. Sina, P. Parikh, T. Uekert, B. Shahbazian, A. Devaraj, Y.S. Meng, Nano Lett. 16 (2016) 5594.
[49] K. Rakstys, A. Abate, M.I. Dar, P. Gao, V. Jankauskas, G. Jacopin, E. Kamarauskas, S. Kazim, S. Ahmad, M. Grätzel, M.K. Nazeeruddin, J. Am. Chem. Soc. 137 (2015), 16172.
[50] T. Leijtens, T. Giovenzana, S.N. Habisreutinger, J.S. Tinkham, N.K. Noel, B.A. Kamino, G. Sadoughi, A. Sellinger, H.J. Snaith, ACS Appl. Mater. Interfaces 8 (2016) 5981.
[51] K. Odysseas Kosmatos, L. Theofylaktos, E. Giannakaki, D. Deligiannis, M. Konstantakou, T. Stergiopoulos, Methylammonium chloride: a key additive for highly efficient, stable, and up-scalable perovskite solar cells, Energy Environ. Mater. 2 (2019) 79–92.
[52] M. Kim, G.H. Kim, T.K. Lee, I.W. Choi, H.W. Choi, Y. Jo, Y.J. Yoon, J.W. Kim, J. Lee, D. Huh, H. Lee, S.K. Kwak, J.Y. Kim, D.S. Kim, Joule 3 (2019) 2179.
[53] F. Zheng, C. Zuo, M. Niu, C. Zhou, S.J. Bradley, C.R. Hall, W. Xu, X. Wen, X. Hao, M. Gao, T.A. Smith, K.P. Ghiggino, ACS Appl. Mater. Interfaces 12 (2020), 25980.
[54] K.T. Cho, O. Trukhina, C. Roldán-Carmona, M. Ince, P. Gratia, G. Grancini, P. Gao, T. Marszalek, W. Pisula, P.Y. Reddy, T. Torres, M.K. Nazeeruddin, Adv. Energy Mater. 7 (2017) 1.
[55] S.A. Odom, K. Lancaster, L. Beverina, K.M. Lefler, N.J. Thompson, V. Coropceanu, J.L. Bredas, S.R. Marder, S. Barlow, Chem. A Eur. J. 13 (2007) 9637.
[56] S.H. Kang, I.T. Choi, M.S. Kang, Y.K. Eom, M.J. Ju, J.Y. Hong, H.S. Kang, H.K. Kim, J. Mater. Chem. A 1 (2013) 3977.